This manuscript was accepted by J. Appl. Phys. Click here to see the version of record.

Chemical Speciation of U, Fe, and Pu in Melt Glass from Nuclear Weapons Testing

J.I. Pacold, W. W. Lukens, C.H. Booth, D.K. Shuh

Chemical Sciences Division, Lawrence Berkeley National Laboratory, Berkeley, CA, 94720, USA

K.B. Knight, G.R. Eppich

Nuclear and Chemical Sciences Division, Lawrence Livermore National Laboratory, Livermore, CA 94550, USA

K.S. Holliday

Materials Science Division, Lawrence Livermore National Laboratory, Livermore, CA 94550, USA

(Dated: April 25, 2016)

Nuclear weapons testing generates large volumes of glassy material that influence the transport of dispersed actinides in the environment and may carry information on the composition of the detonated device. We determine the oxidation state of U and Fe (which is known to buffer the oxidation state of actinide elements and to affect the redox state of groundwater) in samples of melt glass collected from three U.S. nuclear weapons tests. For selected samples, we also determine the coordination geometry of U and Fe, and we report the oxidation state of Pu from one melt glass sample. We find significant variations among the melt glass samples, and in particular, find a clear deviation in one sample from the expected buffering effect of Fe(II)/Fe(III) on the oxidation state of uranium. In the first direct measurement of Pu oxidation state in a nuclear test melt glass, we obtain a result consistent with existing literature that proposes Pu is primarily present as Pu(IV) in post-detonation material. In addition, our measurements imply that highly mobile U(VI) may be produced in significant quantities when melt glass is quenched rapidly following a nuclear detonation, though these products may remain immobile in the vitrified matrices. The observed differences in chemical state among the three samples show that redox conditions can vary dramatically across different nuclear test conditions. The local soil composition, associated device materials, and the rate of quenching are all likely to affect the final redox state of the glass. The resulting variations in glass chemistry are significant for understanding and interpreting debris chemistry, and the later environmental mobility of dispersed material.

I. INTRODUCTION

The chemical state of radionuclides in the environment is of considerable interest due to its effects on transport [1–7]. Heavy elements such as actinides contained in solutions and in crystalline

ing particulate matrices may be incorporated into groundwater as solutions and colloids, leading to migration over km distances [8–10]. The selection of suitable hosts for waste materials must take into account the possibility of release of materials into the environment under wet conditions [11]. Many studies of transport therefore are motivated by issues related to the storage of high-level nuclear waste and utilize highly characterized model waste forms. The migration of actinides at historical test sites has been relatively well studied [1, 4, 12–15] compared with the limited literature on the parameters that may affect the relative mobility of actinides and fission products in vitrified, macro-scale debris [16–18]. An understanding of the specific melt glass forms produced by underground and near-surface weapons testing is important for prediction and remediation of contaminant plumes at sites where nuclear testing has occurred. In addition, melt glass can retain a record of chemical signatures of the detonation, including residual actinides from the device [19, 20]. For example, studies have shown that analyses of fission product relationships can be useful to constrain the chemical fractionation processes in fallout, and are characteristic of the nuclear event [21, 22].

The processes that take place following a nuclear explosion are briefly summarized here. During the first few milliseconds after ignition of a near-surface nuclear test, the device components and some of the surrounding rock and soil are vaporized. In underground tests [23, 24], the superheated vapor expands, forming a cavity in the surrounding rock. Small amounts of material may condense before making contact with the surfaces of the cavity, forming vitreous materials. The cavity collapses, forming a chimney of fractured rock, and molten material collects at the bottom of the chimney, solidifying into a large mass of melt glass over several days. In surface and near-surface tests [23, 24], on the other hand, a plume of vaporized device material and rock is released into the atmosphere. Melt glass can be formed in situ (directly on the surface), as well as through the melting of material pulled into the hot plume. Residual actinides from unburned fuel and associated device materials are typically present in the melt glass at μg/g concentrations [20].

We focus here on the mobility of residual U and Pu. The environmental reactivity of these species in macro-scale melt glasses is not yet understood, and the existing literature on actinide transport implies that it will depend on both the composition of the glass itself and on environmental conditions. In general, U(VI) and Pu(VI) as the uranyl (UO_2^{2+}) and plutonyl (PuO_2^{2+}) ions are relatively soluble and mobile in water, while U(IV) and Pu(IV) tend to sorb to mineral surfaces [25, 26]. This does not necessarily mean that the tetravalent ions are immobilized. Depending on the groundwater chemistry and the mineral and organic species present in the local environment, both U(IV) and Pu(IV) can be incorporated into aqueous colloids [5, 27, 28] or U(IV) may be con-

ngted into U(VI) by weathering [29]. In the case of bulk melt glass, the redox state of the material may impact the redox state of groundwater flowing through the test location [30, 31], affecting, in turn, the solubility and transport properties of other materials. Therefore, the chemical state of both the actinides and the glassy matrix may strongly influence the source terms used in transport models.

There have been extensive analyses of redox chemistry in synthetic U- and Pu-bearing waste-form silicate glasses [32–40]. However, information on the redox state of detonation-produced melt glasses is limited. An early analysis of products from two tests at the Nevada National Security Site (NNSS) [16] found that Fe provides a possible signature of reducing conditions during the detonation of a nuclear weapon. Specifically, the Fe(II)/Fe(III) ratio in melt glass is generally higher than in the surrounding rock and soil. It is also important to note that transition metals, including Fe, can act as buffers for the redox state of U and Pu in silicate glasses [40–42]. To our knowledge, the only further studies in this direction have been two evaluations of Fe oxidation states in fallout glass from the Trinity site [43, 44] and a comparison of Fe and U oxidation states in synthetic melt glasses with specimens collected from the NNSS [30]. In these studies, X-ray absorption near edge structure (XANES) was used to nondestructively determine the bulk-averaged oxidation states of the elements of interest. Other lines of recent evidence based on fission product behaviors [18] also indicate that reducing conditions may have prevailed in at least some nuclear events.

Here, we use XANES to evaluate the oxidation state of U and Fe in melt glass samples from three different U.S. nuclear weapons tests; for one specimen, we also determine the oxidation state of Pu. Where possible, we measure the local atomic structure with extended X-ray absorption fine structure (EXAFS) spectroscopy to further clarify the chemical state of U and Fe. We expand on the existing published XANES studies by (1) characterizing melt glasses produced by tests performed under several disparate conditions, (2) determining the Pu oxidation state in one sample, and (3) using the local structure information provided by EXAFS to derive further constraints on the possible Fe and U species present. Section II describes sample collection, data collection, and data analysis procedures. Section III presents XANES and EXAFS results. In Section IV, these results are compared with literature information on synthetic silicate melt waste forms. In Section V, we summarize and conclude with some hypotheses on the effects of quenching timescales that may explain our observations, and discuss the implications for the interpretation of the chemical record preserved in fallout melt glasses.

II. MATERIALS AND METHODS

We analyzed melt glass samples produced by three nuclear test events, and soils collected proximate to two of the tests. "Event 1" melt glass is derived from a primarily U-fueled event containing some Pu. A sample of melt glass was collected by drilling into the fractured rock chimney. "Event 2" melt glass is derived from a near-surface event, primarily Pu-fueled and containing some U. "Event 3" melt glass is from a near-surface, primarily U-fueled event. To obtain the two near-surface samples, soil within 10 cm of the surface in the area proximate to the test ground zero was sieved to collect ∼1 mm-diameter glassy particles for analysis. Glasses were selected from the sieved soils by inspection with an optical microscope (see ref. [20] for descriptions of similar glasses). Samples of local soils were also collected from the areas near Event 2 and Event 3, away from the ground zero and the area affected by the fallout plume at each location.

Fallout melt glass samples for Fe, U, and Pu concentration analysis were washed using 18.2 MΩ H_2O and dried. Samples were digested in clean Teflon beakers using an approximately 2:1 mixture of concentrated HNO_3 to concentrated HF at a temperature sufficient to fully dissolve each sample, approximately 110 °C. United States Geological Survey rock standard RGM-1, utilized here as a standard to assess compositional data accuracy, was dissolved alongside the glass samples using the same procedures. Samples were heated at ∼110 °C for at least 24 hours, until a white fluoride precipitate formed. At this point, ∼1 mL concentrated $HClO_4$ was added to each beaker to dissolve the fluoride precipitate. Samples were then dried, dissolved in ∼1 mL concentrated HCl, and dried again. Finally, samples were dissolved in ∼5 mL 3 M HCl, with no residual solid fractions remaining. The 3 M HCl solutions were used to determine Fe, U, and Pu concentrations by inductively coupled plasma mass spectrometry (ICP-MS), following the methods of ref. [20]. In brief, aliquots of the solutions were transferred to a separate set of Teflon beakers, dried, and dissolved and dried twice in concentrated HNO_3 to remove residual chloride. The precipitates were then dissolved in a solution of 2% HNO_3 containing 5 ng/g ^{6}Li, ^{45}Sc, ^{115}In, and ^{209}Bi for internal standardization of quadrupole ICP-MS measurements. Major and trace element concentrations were measured using either a Thermo iCAP-Q quadrupole ICP-MS, Thermo X-Series quadrupole ICP-MS, or Thermo Element II SF-ICP-MS. Concentrations were quantified using matrix-matched calibration curves for the elements of interest, including Fe, U, and Pu. Elemental concentrations were calculated based on measured signal intensities relative to the known concentrations of the calibration standards.

For X-ray absorption spectroscopy measurements, each melt glass and soil sample was ground

in a mortar, and the resulting powders were used to fill aluminum sample brackets with internal volumes of approximately 0.25 cm^3. XANES and EXAFS data were collected at beamline 11-2 of the Stanford Synchrotron Radiation Lightsource (SSRL). Due to the low concentrations of Fe, U, and Pu present, spectra were collected in fluorescence mode, using a 100-element Ge detector. Fe K-edge XANES and EXAFS data were obtained for all three melt glass samples, both soil samples, and three Fe(II)-bearing materials (staurolite, grandidierite, and tektite). Low U and Pu concentrations limited the quality of U and Pu L_{III}-edge data that could be obtained. Low-noise U L_{III} EXAFS data were collected from the Event 3 glass, and Pu L_{III}-edge XANES from the Event 2 sample. XANES data were also collected in transmission mode from a set of reference powders: metallic Fe, FeO, Fe_3O_4, and α-Fe_2O_3 at the Fe K-edge; UO_2, UF_4, and uranyl acetate at the U L_{III}-edge; and PuO_2 at the Pu L_{III}-edge. The energy scales were calibrated by setting the energy of the Fe K edge measured from an Fe metal powder to 7111.8 eV, setting the energy of the U L_{III}-edge of the UO_2 powder to 17166.0 eV, and setting the energy of the Pu L_{III}-edge of the PuO_2 powder to 18043.5 eV. Data analysis was performed with the RSXAP software package [45–47]. Standards for fits to the EXAFS data were calculated using FEFF8 [48]; errors in the reported fit parameters were calculated using a Monte Carlo method [49], and represent one standard deviation from the best fit value. Each error is calculated by fixing the relevant parameter and allowing the others to float until the reduced chi-squared value increases by one. Correlations between the fit parameters (e.g., between coordination numbers and Debye-Waller factors) are therefore reflected in the reported errors.

III. RESULTS

The concentrations of Fe, U, and Pu in the melt glass samples and in soils collected proximate to Events 2 and 3 are given in Table I. Fe K-edge XANES collected from the three melt glass samples and the two soil specimens, as well as reference Fe oxides and minerals, are shown in Figs 1 and 2. Spectra are pre-edge background-subtracted and normalized to the average signal in the post-edge region between 7150 eV and 7250 eV. The energy at "half-height," i.e., the energy at which the absorption coefficient reaches half of the edge step, is empirically linearly dependent on the bulk-averaged Fe oxidation state. This allows us to estimate the oxidation state of the soil and glass samples by interpolation between the half-height energies of the oxides. Results are given in Table II. For the two events for which it was possible to obtain control soil samples, the XANES results show drastic Fe reduction.

Reduction of iron during melt glass formation can also be observed by examining the pre-edge peaks shown in Fig. 1 (right) and Fig. 2 (right). XANES studies of Fe-bearing minerals and glasses, including waste-form glasses and fallout collected from the Trinity test [50–57], often use the centroid of the pre-edge peaks (after isolation from the background) to quantitatively determine the Fe(II)/(Fe(II) + Fe(III)) fraction. The results of applying this procedure to our dataset are shown in Fig. 3. We do not use this approach to quantify the Fe(II) fraction here, since the pre-edge features are also highly sensitive to coordination geometry [55, 58] and spin state [59]. In particular, we note that this method gives nearly identical oxidation states for Fe_3O_4 and Fe_2O_3. The centroid results are, however, qualitatively consistent with the edge shift results, and the pre-edge features support the conclusion that Fe(III) in the associated soils is reduced to Fe(II) in the melt glasses.

We confirm the predominance of Fe(II) in the melt glasses by examining the Fe coordination. To suggest possible structural models, we first qualitatively compare the melt glass samples with minerals having known Fe speciation. In Fig. 4, the k-space Fe K-edge EXAFS collected from the soil and glass samples are shown with spectra collected from staurolite, containing 4-coordinate Fe(II) [55]; grandidierite, containing approximately 90% 5-coordinate Fe(II) and 10% Fe(III) [60]; and a tektite from the Australasian strewnfield [61]. Tektites have been proposed as naturally occurring analogs to nuclear melt glass [56, 57], and are reported to predominantly contain Fe(II) in distorted tetrahedral coordination [43, 62, 63].

Fig. 5 and Table III show EXAFS fitting results. For analysis of the melt glass spectra, we restricted the fit to the range of 1.0 Å $< R <$ 3.0 Å and used only two coordination shells. Attempting to add further oxygen coordination shells reduces the number of degrees of freedom and yields less reliable fits. The same fitting procedure was then applied to the soil and tektite data. For all three glass specimens, we obtain a coordination number of ∼3 and a bond length of ∼1.9 Å for the first shell. The low coordination number for the second shell is consistent with the expected amorphous nature of the material. The soil samples show higher coordination numbers, with large uncertainties in the second shell coordination number; this is consistent with the presence of a mixture of igneous Fe-Ti oxide minerals in NNSS soil [20]. For the tektite, we obtain a coordination number of ∼3, with a bond length of ∼2.0 Å. Applying the two-shell fitting procedure to staurolite and grandidierite yields poor results, as there is a complex series of coordination shells between 2.5 Å and 3.5 Å from the Fe sites in each mineral [60, 64]. We therefore follow ref. [60] by fitting only the first shell over a range of 1.0 Å $< R <$ 2.0 Å. This yields coordination numbers of ∼3 for 4-coordinate staurolite and ∼5 for primarily 5-coordinate grandidierite. Overall, these results

confirm that Fe in the melt glasses is predominantly 4-coordinate Fe(II). The bond lengths observed for the melt glasses and tektite are near the endpoints of the previously reported range for tektites collected from various strewnfields [52, 63].

Uranium L_{III}-edge XANES collected from the three melt glass samples, two U(IV) compounds, and one U(VI) (uranyl) compound are shown in Fig. 6. U(V), by analogy with Np(V), should have a slightly negative shift of the white line position compared to that of U(IV) [65]. Given the positive shifts of the white line relative to that of UO_2, all three samples display bulk-averaged oxidation states intermediate between U(IV) and U(VI), with the Event 3 glass containing the largest fraction of U(VI). The measured white line shifts are given in Table IV, together with bulk-averaged oxidation states estimated by interpolating linearly between the white lines of the reference compounds. We note that in principle it should be possible to obtain a more accurate estimate by decomposing the melt glass spectra into linear combinations of the U(IV) and U(VI) reference spectra. However, the post-edge features in the melt glass spectra (centered near 17190 eV) cannot be reliably fit with this approach. In addition, our simple linear interpolation implicitly assumes that the quantity of U(V) present is negligible [66]. Keeping these systematic uncertainties in mind, we estimate U(VI)/(U(IV) + U(VI)) fractions of ∼32% for the Event 1 and Event 2 glasses, and ∼84% for the Event 3 glass.

The U content of the Event 1 and Event 3 glasses was sufficiently high for collection of EXAFS data in addition to the XANES (Fig. 7), though the noise level of the Event 1 data leads to large uncertainties in the extracted coordination numbers. Fourier-transformed EXAFS data and fit results are shown in Fig. 8, and the fit parameters are given in Table V. For ∼60% of the uranium in the Event 3 glass, we find one coordination shell with a bond length of ∼1.77 Å, consistent with the axial U-O bonds in the uranyl U(VI) ion [65]. The small value of σ^2 is qualitatively consistent with a nearly undistorted uranyl coordination. U(V) may be present in glassy materials [37, 42, 67], and in this case a small amount of U(V) (which should have a U-O_{ax} distance of about 1.83 Å [65]) is possible, especially given the slightly enhanced σ^2 value of 0.006 Å^2, where more typically $\sigma^2_{\text{U-O}_{ax}} \approx 0.0015$ Å^2. However, since uranyl coordination in a pure compound is 2, these data indicate 60 ± 10% of the uranium in the sample is in uranyl-like bonding environments, mostly as U(VI). The second shell contains 3.5±0.5 atoms at 2.28±0.1 Å, consistent with equatorially coordinated oxygens, but also possibly containing contributions from a U(IV) phase.

A Pu L_{III}-edge XANES spectrum was also collected from the Event 2 sample, and closely matches that of PuO_2 (Fig. 9). All three samples contain Zr, and the Zr K edge (approximately 60 eV below the Pu L_{III} edge) contributes a significant background. While the Event 1 melt glass

contained some Pu (Table I), a low signal-to-background ratio made it impractical to collect Pu L_{III}-edge XANES in this sample.

IV. DISCUSSION

The data allow for several observations regarding the variations in the oxidation states of Fe and U in samples formed under different nuclear testing conditions. For this discussion, we assume that the U and/or Pu associated with each event was in a metallic form prior to detonation. The XANES data acquired from the soil samples indicate that the Fe present in the surrounding rock and soil contributed a large quantity of Fe(III) in oxide form to the melt glasses. We observe oxidation of U to a mixture of U(IV) and U(VI) in all three melt glasses, with a larger fraction of U(VI) in the Event 3 sample; our assumptions and observations concerning the change in average oxidiation state of each species are summarized in Fig. 10. It is curious that the U-fueled event (Event 3), which under our assumptions would have had the largest quantity of metallic U present before detonation, records the most oxidized uranium in the resulting melt glass. The Pu in the Event 2 sample is predominantly oxidized to Pu(IV).

The iron in the melt glass is present as reduced Fe(II) in all three samples. Structural and diagnostic equipment associated with a nuclear weapons test may contribute an appreciable mass of metallic iron to the resultant debris. This would likely have been most significant in underground testing, where device and associated structure and diagnostics can contribute a few tenths of a weight percent Fe to the melt glass [16]. In this case, one might predict that the melt glass from the underground test (Event 1) would record the most reduced Fe, because of the significant contribution of metallic Fe before detonation. In these samples, however, the sample that shows the most reduced Fe is derived from the near-surface U fueled test (Event 3). This may imply that considerable metallic iron was available as a tower or diagnostics-related equipment to Event 3, but further conclusions cannot be made from these data alone.

In synthetic melt glasses, Fe acts as a buffer for U [40–42]. However, the Event 3 glass in the present study contains more reduced Fe and oxidized U in comparison with the Event 1 and Event 2 glasses. The observed variation between melt glass samples from different events may be attributed to the differences in initial conditions, respective cooling rates, and/or the non-equilibrium redox conditions produced by a nuclear detonation. A nuclear explosion can produce an initial plasma largely devoid of oxygen (highly reducing conditions), and as noted above, may mix metallic Fe from the device and/or associated structure in with the oxidized Fe contained in the surrounding

melt. Recent studies have shown that aerodynamic fallout that has likely quenched in atmosphere cools to a glass on time scales of seconds [18]. We hypothesize that this short cooling time scale inhibits the expected Fe/U buffering effect by locking in the oxidation states of Fe and U before local oxygen fugacity can have any significant effect (as in the production of synthetic glasses under equilibrium conditions). Weathering driving U(IV) towards U(VI) [29] may be another explanation for the high U(VI) content of the Event 3 glass; we cannot rule out such effects based on the present data alone, but note that for similar melt glasses [18], reported step-heated gas extraction patterns are inconsistent with any significant disturbances due to weathering effects.

The uranium associated with the device is likely to be ionized by the high temperatures reached at the center of the detonation, typically over 10^7 K [17, 23, 68]. We therefore assume that uranium initially condenses and is incorporated into the glass as U(VI), the most highly ionized state observed in solid U-O phases [69, 70]. Under this hypothesis, we might interpret Event 3 glass to have been quenched before equilibration between the Fe(II) and U(VI) could occur, while the glasses from Event 1 and Event 2 cooled over a slightly longer time, allowing some Fe(II) oxidation to Fe(III), and corresponding U(VI) reduction to U(IV). It is interesting that the EXAFS-derived bond lengths are inconsistent with the presence of a significant quantity of U(V). While U(V) disproportionates to U(IV) and U(VI) in aqueous solution, it can be a stable oxidation state in silicate glasses [37, 40, 42, 71]. The small fraction of U(V) in the present samples may be due to lower concentrations, relative to synthetic glasses, of redox-sensitive species that can stabilize U(V) (such as Ti [72] and Ce [40]), or may be another effect of the rapid quenching of the melt glass before equilibration with the atmosphere.

For comparison, we note that a previous study of melt glass collected from underground tests [30] reported Fe(II) fractions ranging from 33% to 53%. The fraction of U present in each oxidation state was not quantified, but XANES data qualitatively indicated the presence of a mixture of U(VI) and U(V). One explanation may be that these samples cooled over longer timescales than the samples used in this study, allowing for equilibration and yielding oxidation states similar to those found in synthetic glasses. Melt glass produced by the Trinity test is known to contain Fe predominantly as Fe(II) [43, 44]. Measuring the oxidation states of U and Pu in Trinity melt glass could provide an instructive comparison regarding the influence of both quenching time and structural material on the final redox state of actinides in the glass, as the Trinity test was conducted under well-documented atmospheric conditions in the presence of a steel tower containing metallic iron [73].

To summarize, quenching timescales and the incorporation of device and associated structural

materials, as well as the original oxidation state of the carrier (soil) materials, into the resultant melt glasses are likely to determine the final redox states of Fe and U. Both of these effects would increase the final fraction of Fe(II) in the melt glass, and they must be disentangled in order to draw quantitative conclusions regarding the sources of iron in the melt glass. Spectromicroscopic data may provide more detailed information in this regard, as lectron microscopy studies have observed metal-rich regions with dimensions ranging from nanometers to millimeters in Trinity event debris [19, 74]. In addition, from the point of view of environmental transport, the presence of a large fraction of U(VI) in a uranyl-like bonding environment is quite interesting, since U(VI) as uranyl is the most soluble and mobile oxidation state of uranium [26, 65, 75–77]. In these specimens, however, the uranium is bound in the melt glass, and unlikely to be easily mobilized in its present state.

Finally, we observe that the Pu oxidation state measured in melt glass from Event 2 (Pu(IV), Fig. 9) is consistent with the literature on actinide-bearing silicate glasses. Waste-form glasses synthesized under a wide range of oxygen fugacities contain Pu pre-dominantly as Pu(IV) [35, 78]. The stability of the Pu(IV) oxidation state has been attributed, by some authors, to the presence of large mass fractions of Fe [71]. The Fe(II)/Fe(III) redox couple can stabilize the oxidation state of Pu, since Fe(II) typically oxidizes before Pu(IV), while Fe(III) is typically reduced before Pu(IV). This couple also affects environmental Pu transport mechanisms, since Pu(IV) is relatively insoluble in water, but forms PuO_2 colloids [9, 10] and sorbs to colloidal minerals [79–81]. The encasement of Pu into macroscale glassy matrices, however, may reduce the probability of initial colloid formation, and serve to inhibit the transport of actinides, as observed in waste vitrification studies.

V. SUMMARY

We have determined the bulk-averaged oxidation states of U and Fe in three melt glass samples produced in different nuclear tests: a near-surface U-fueled test, a near surface test containing U and Pu, and an underground test containing U and Pu. We find that Fe is strongly reduced in all three melt glasses, suggesting the incorporation of significant Fe(II) at the time of detonation and/or reduction of Fe(III) to Fe(II) during the formation of the melt glasses. We also found that the U glass from the two mixed-actinide events is a mixture of U(IV) and U(VI). The Fe found in the melt glass from the U-fueled event is almost entirely 4-coordinate Fe(II), while over 60% of the uranium in this sample is U(VI) in a uranyl-like bonding environment.

We have also spectroscopically determined that the oxidation state of Pu in the near-surface Pu-fueled event melt glass is predominantly Pu(IV). Our Pu results corroborate the existing literature on Pu glass synthesis, while our U and Fe results imply that melt glass redox chemistry varies widely depending on test conditions. The presence of the most reduced Fe and oxidized U in the melt glasses from the U fueled test, as compared with the Pu-U fueled and underground tests, suggests that a single oxygen fugacity and redox equilibrium do not apply to melt glasses from nuclear weapons testing. We hypothesize that cooling timescales and the availability of metallic Fe from the device and structure may be primarily responsible for the observed variations. Further information is needed to quantify the relative importance of these two effects and to better understand the relative effects of environmental and anthropogenic sources of iron on the resultant oxidation states of the residual actinides. Differences in the composition of melt glass in contact with groundwater may have considerable consequences for dissolution and transport processes in nuclear debris fields.

VI. ACKNOWLEDGMENTS

We thank Pat Allen and Tim Rose for useful insights and discussion. This work was funded by the Office of Defense Nuclear Nonproliferation Research and Development within the U.S. Department of Energy's National Nuclear Security Administration, under Contract Number DE-AC02-05CH11231 at Lawrence Berkeley National Laboratory and under Contract No. DE-AC52-07NA27344 at Lawrence Livermore National Laboratory. Use of SSRL, SLAC National Accelerator Laboratory, is supported by the U.S. Department of Energy, Office of Science, Office of Basic Energy Sciences under Contract No. DE-AC02-76SF00515.

Sample	Fe weight fraction	U weight fraction	Pu weight fraction
Event 1 glass	$(1.18 \pm 0.38) \times 10^{-2}$	$(4.1 \pm 0.9) \times 10^{-6}$	$(0.05 \pm 0.03) \times 10^{-6}$
Event 2 soil	$(2.20 \pm 0.23) \times 10^{-2}$	$(2.3 \pm 0.3) \times 10^{-6}$	-
Event 2 glass	$(2.61 \pm 0.36) \times 10^{-2}$	$(13.9 \pm 9.8) \times 10^{-6}$	$(13.43 \pm 9.65) \times 10^{-6}$
Event 3 soil	$(2.22 \pm 0.13) \times 10^{-2}$	$(2.9 \pm 0.1) \times 10^{-6}$	-
Event 3 glass	$(2.29 \pm 0.17) \times 10^{-2}$	$(24.9 \pm 7.6) \times 10^{-6}$	-

TABLE I: Weight fractions of Fe, U, and Pu in the melt glass samples and in soil samples collected proximate to Events 2 and 3. Pu was not detected in the soils or in the Event 3 glass (the expected detection limit is 0.1 ppt). Each reported uncertainty is the standard deviation of the mean of all measurements obtained from a single sample. Between 3 and 70 measurements were obtained from each sample, depending on the quantity of material available.

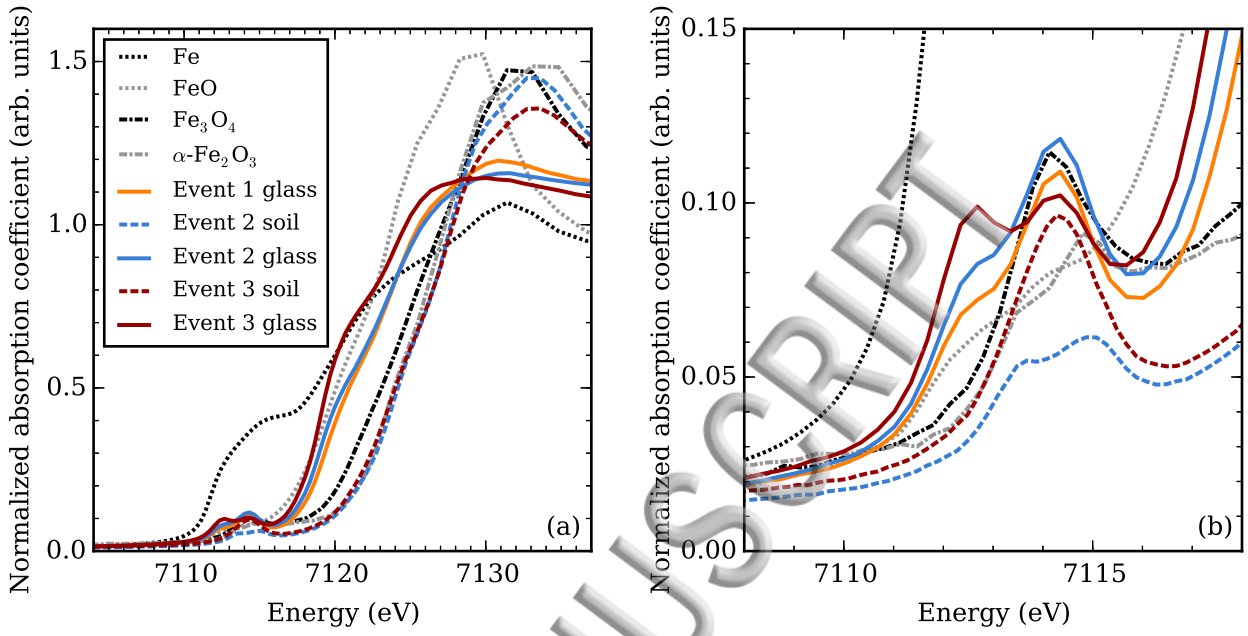

FIG. 1: (a) Fe K-edge XANES of Fe metal, Fe(II) oxide, Fe(II,III) oxide, Fe(III) oxide, and melt glass samples. (b) Pre-edge region.

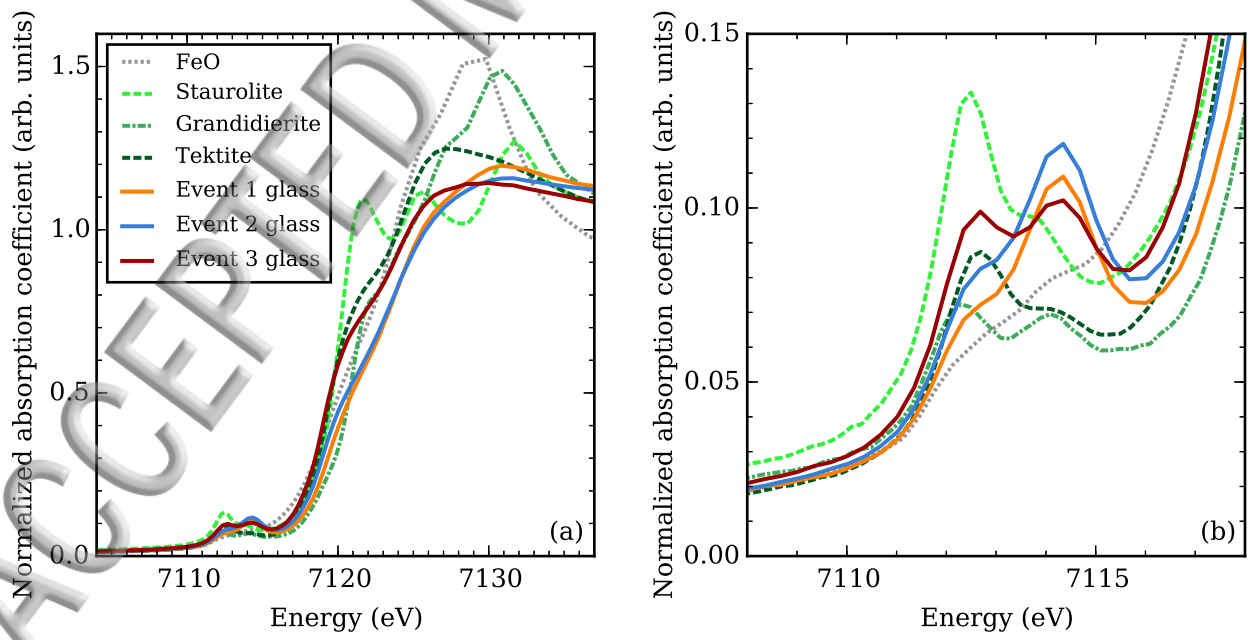

FIG. 2: (a) Fe K-edge XANES of nominally divalent Fe standards, soils, and melt glasses. (b) Pre-edge region. Note that grandidierite contains approximately 90% Fe (II) and 10% Fe(III).

Sample	Edge energy at half-height	Nominal oxidation state	Measured oxidation state
FeO	7120.13	2	2.02
Fe_3O_4	7123.13	2.67	2.71
Fe_2O_3	7124.17	3	2.95
Staurolite	7119.70	2	1.92
Grandidierite	7120.89	2.1	2.20
Tektite	7120.10	-	1.92
Event 1 glass	7120.80	-	2.18
Event 2 soil	7125.04	-	3.15
Event 2 glass	7120.47	-	2.10
Event 3 soil	7124.35	-	2.99
Event 3 glass	7119.46	-	1.87

TABLE II: Average oxidation states of Fe in soils, melt glass samples, and reference minerals determined by linear interpolation of Fe K-edge half-height. The estimated uncertainty in the calculated oxidation states is ±0.07 (due to error in the linear fit to the reference oxide materials).

This manuscript was accepted by J. Appl. Phys. Click here to see the version of record.

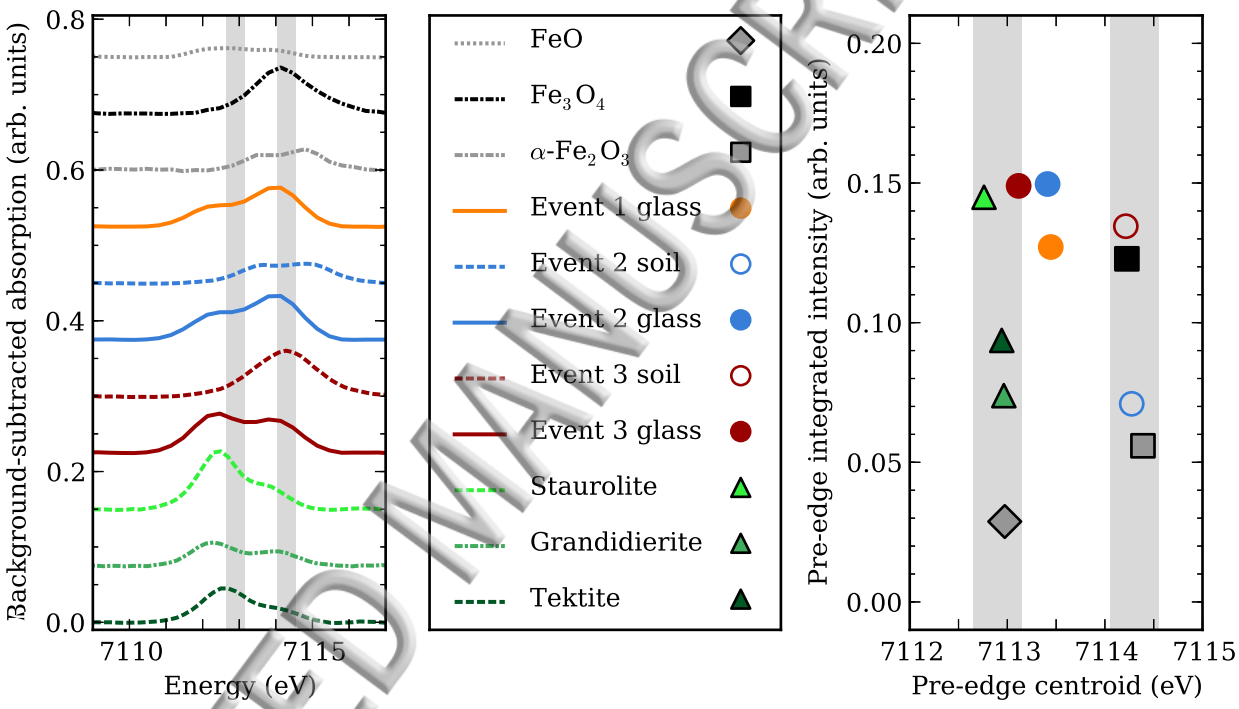

FIG. 3: Fe K-edge pre-edge XANES for reference Fe materials, soils, and melt glasses. A cubic spline background has been subtracted from each spectrum. Centroids and integrated intensities are shown in the right panel. The shaded bands in each plot correspond to the commonly used range of centroid energies [53–57] corresponding to Fe(II) (lower energy) and Fe(III) higher energy.

This manuscript was accepted by J. Appl. Phys. Click here to see the version of record.

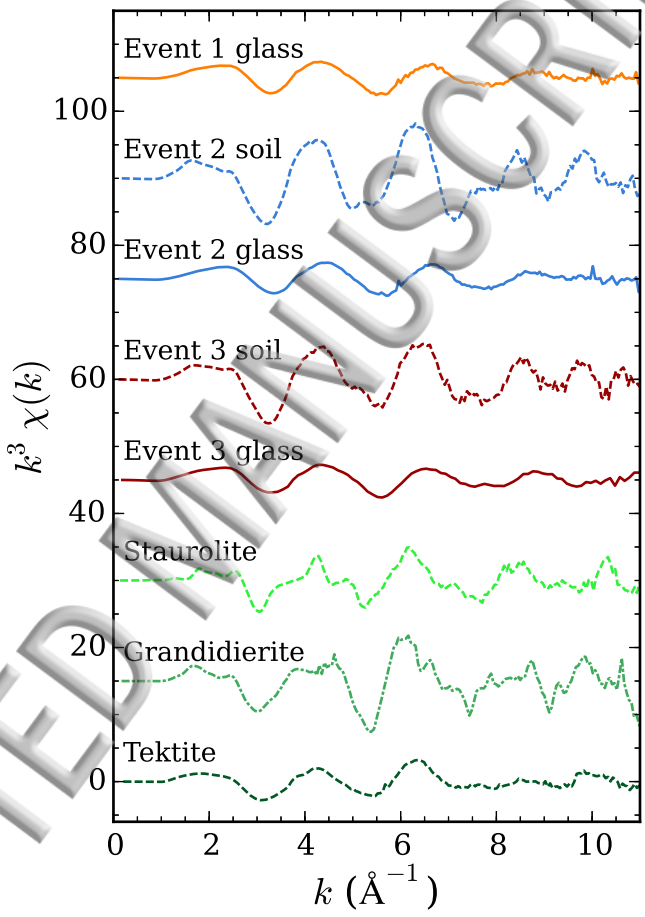

FIG. 4: Fe K-edge EXAFS collected from melt glass samples and Fe-bearing reference minerals.

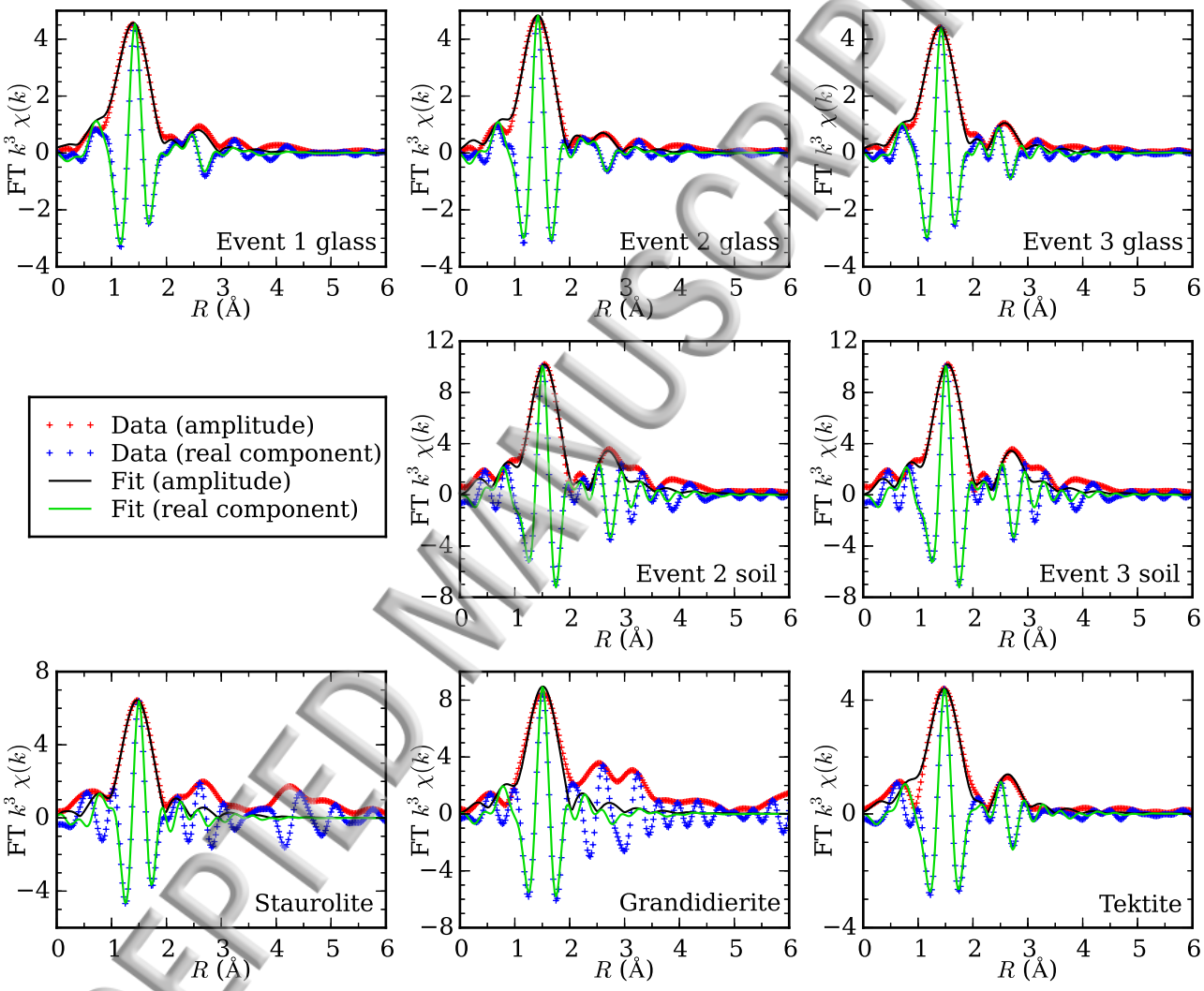

FIG. 5: Fourier-transformed Fe K-edge EXAFS and fit results for the melt glass samples, soils, and Fe(II)-bearing minerals. Fits were performed for 1.0 Å $< R <$ 3.0 Å, with the exceptions of staurolite and grandidierite, for which the fit range was restricted to 1.0 Å $< R <$ 2.0 Å following ref. [60].

This manuscript was accepted by J. Appl. Phys. Click here to see the version of record.

	Event 1 glass			Event 2 glass			Event 3 glass		
Path	N	R (Å)	σ^2 (Å^2)	N	R (Å)	σ^2 (Å^2)	N	R (Å)	σ^2 (Å^2)
Fe-O	3.1(2)	1.90(1)	0.011(1)	2.6(1)	1.91(1)	0.008(1)	2.7(1)	1.90(1)	0.009(1)
Fe-Fe	0.5(6)	2.94(3)	0.01(1)	0.5(9)	2.92(5)	0.02(1)	0.3(2)	2.94(2)	0.005(5)
ΔE_0	1.9(15)			-1.3(13)			-0.2(15)		
R(%)	8.20			7.94			9.03		
				Event 2 soil			Event 3 soil		
Path				N	R (Å)	σ^2 (Å^2)	N	R (Å)	σ^2 (Å^2)
Fe-O				5.1(5)	2.01(1)	0.006(1)	4.4(5)	1.98(1)	0.008(1)
Fe-Fe				0.9(12)	3.03(1)	0.003(5)	2.3(40)	3.03(2)	0.02(1)
ΔE_0				-4.8(16)			-5.0(19)		
R(%)				11.51			13.17		
	Staurolite			Grandidierite			Tektite		
Path	N	R (Å)	σ^2 (Å^2)	N	R (Å)	σ^2 (Å^2)	N	R (Å)	σ^2 (Å^2)
Fe-O	3.1(7)	1.96(1)	0.004(2)	4.9(10)	1.99(2)	0.007(2)	3.0(3)	1.98(1)	0.010(1)
Fe-Fe	-	-	-	-	-	-	0.5(4)	3.00(2)	0.005(5)
ΔE_0	3.8(35)			-1.2(36)			-1.5(20)		
R(%)	15.57			15.78			12.06		

TABLE III: Fe K-edge EXAFS fit parameters for the melt glass samples, soils, and Fe(II) materials (Fig. 5). An estimate of 0.75 was used for S_0^2 in determining the reported coordination numbers N [82]. The fit range used was 1.0 Å $< R <$ 3.0 Å except in the cases of staurolite and grandidierite, for which the fit range was 1.0 Å $< R <$ 2.0 Å. In all cases, the k^3-weighted data were transformed between 2.5 Å^{-1} and 10.0 Å^{-1}, and Gaussian narrowed by 0.3 Å^{-1}. Stern's rule [83] gives an estimate of 11.6 possible independent parameters for the fits to the glass, soil, and tektite data; the fits reported here have 4.6 degrees of freedom. The staurolite and grandidierite data allow 6.8 independent parameters and the fits have 2.8 degrees of freedom.

This manuscript was accepted by J. Appl. Phys. Click here to see the version of record.

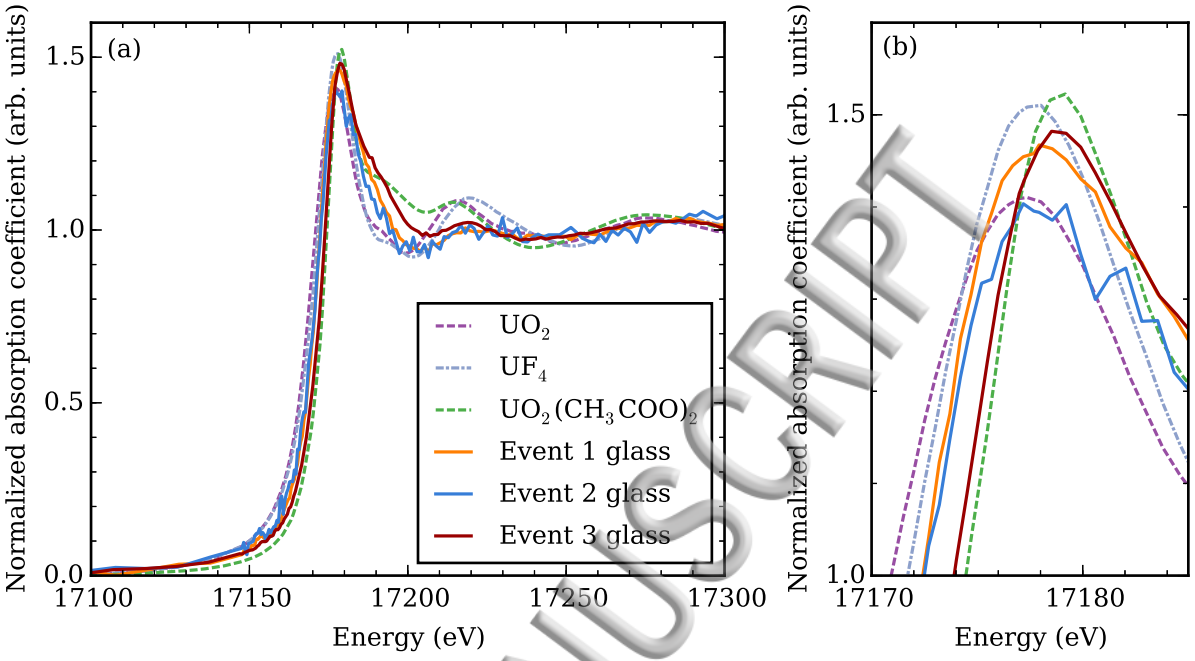

FIG. 6: (a) U L_{III}-edge XANES of reference U(IV) compounds, uranyl acetate, and melt glass samples. Magnification of the white line peaks in (a).

Sample	White line (eV)	Nominal oxidation state	Measured oxidation state
UO_2	17177.2 + 0.0	4	3.8
UF_4	+ 0.3	4	4.2
$UO_2(CH_3COO)_2$	+ 1.9	6	6.0
Event 1 glass	+ 0.7	-	4.6
Event 2 glass	+ 0.8	-	4.7
Event 3 glass	+ 1.6	-	5.7

TABLE IV: U L_{III}-edge white line shifts and corresponding estimated oxidation states for reference U compounds and melt glasses. Peak positions were determined by fitting a Gaussian to an 8 eV-wide band centered on the white line. The uncertainty in the estimated oxidation states, including the error in the peak fitting procedure and the linear fit to the white line positions of the standards, is ±0.2. Note that there are systematic uncertainties in this approach, particularly due to the assumption that a negligible amount of U(V) is present. These uncertainties are mitigated by the more precise information on U speciation obtained from the EXAFS data on the Event 3 glass (further discussed in the text).

This manuscript was accepted by J. Appl. Phys. Click here to see the version of record.

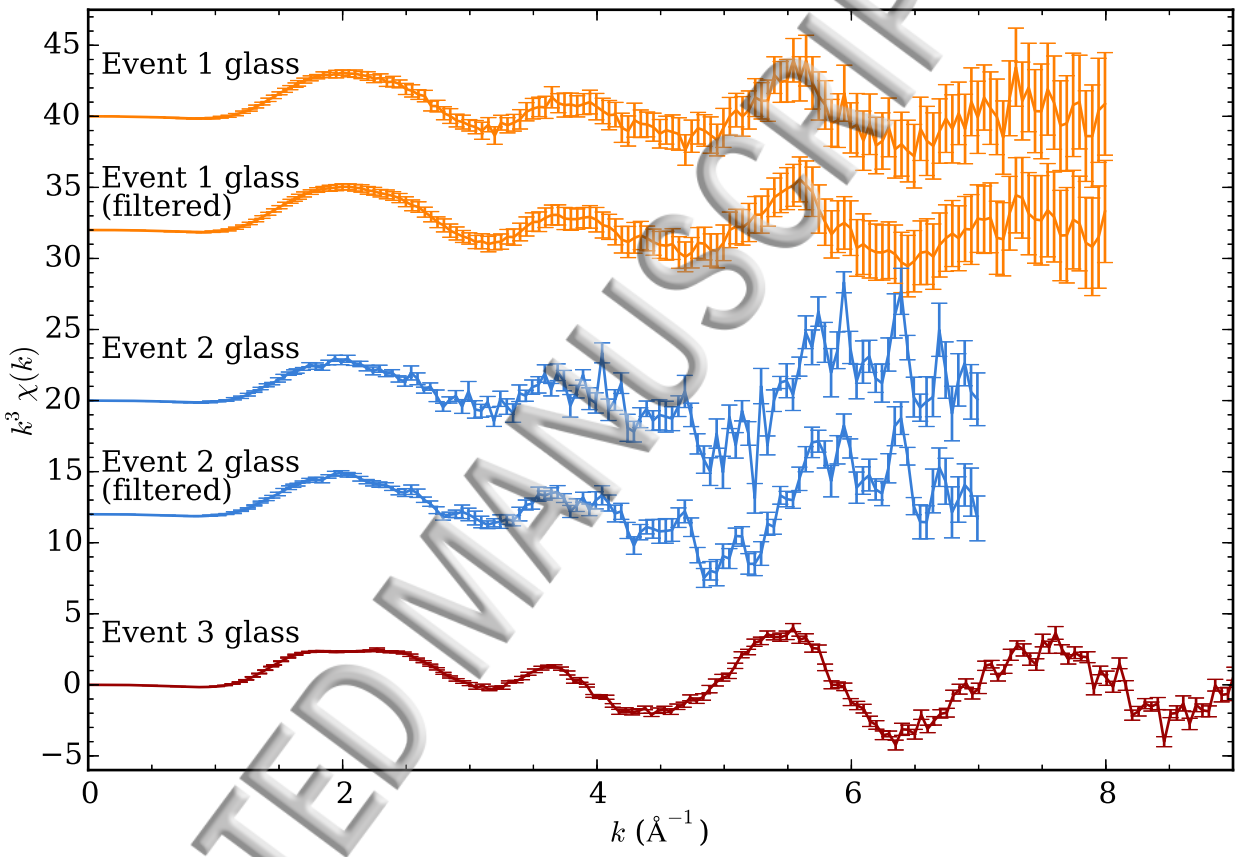

FIG. 7: U L_{III}-edge EXAFS collected from the melt glass samples. For each sample, approximately 5 hours of data collection time were used to acquire a set of between 17 and 20 EXAFS scans. The figure displays the average of each set of scans, with errors estimated as the standard deviation of the mean. The data have been truncated due to low signal-to-noise ratios at higher k. For the Event 1 glass and Event 2 glass, Savitzky-Golay filtered data ($n_L = n_R = 2$) are also shown.

This manuscript was accepted by J. Appl. Phys. Click here to see the version of record.

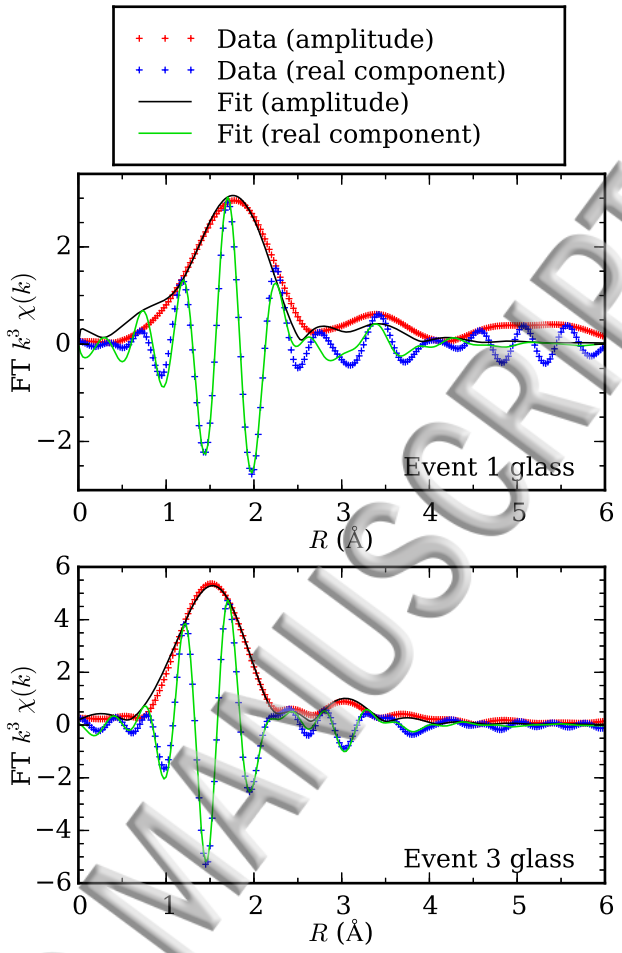

FIG. 8: Fourier-transformed U L_{III}-edge EXAFS, Event 1 and Event 3 glass samples. Note that the data have been Fourier transformed between 2.5 Å^{-1} and 8.0 Å^{-1} for the Event 1 glass and between 2.5 Å^{-1} and 9.0 Å^{-1} for the Event 3 glass (see Fig. 7).

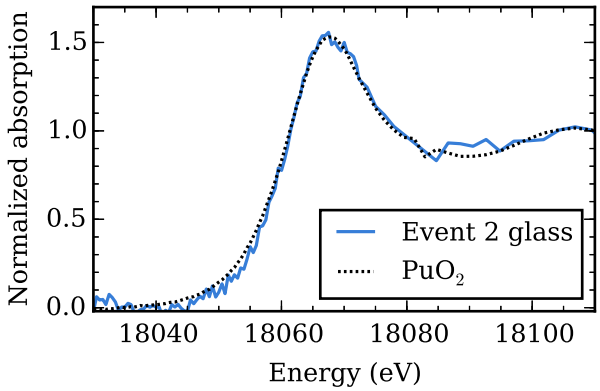

FIG. 9: Pu L_{III}-edge XANES, Event 2 glass and PuO_2.

This manuscript was accepted by J. Appl. Phys. Click here to see the version of record.

	Event 1 glass			Event 3 glass		
Path	N	R(Å)	σ^2(Å^2)	N	R(Å)	σ^2(Å^2)
U-O$_{ax}$	0.6(2)	1.80(1)	0.000(0)	1.2(2)	1.766(8)	0.0006(6)
U-O	3.(1)	2.29(2)	0.007(5)	3.5(4)	2.273(9)	0.008(2)
U-O$_{ax}$-U-O$_{ax}$	1.2	3.60	0.000	2.5	3.533	0.0024
ΔE_0	-17.8(22)			-13.3(12)		
R(%)	18.58			6.35		

TABLE V: Parameters determined in the U EXAFS fits for the Event 1 and Event 3 glasses (Fig. 8). An estimate of 0.9 was used for S_0^2 in determining the reported coordination numbers N [65]. Errors are not reported in the fit parameters for the U-O$_{ax}$-U-O$_{ax}$ scattering path, since these were constrained to twice the corresponding values for the U-O$_{ax}$ path. The fit range used was 1.0 Å $< R <$ 4.0 Å. The k^3-weighted data were transformed between 2.5 Å^{-1} and 8.0 Å^{-1} for the Event 1 glass and between 2.5 Å^{-1} and 9.0 Å^{-1} for the Event 3 glass, and Gaussian narrowed by 0.3 Å^{-1}. For the Event 1 glass data, Stern's rule [83] gave an estimate of 12.5 independent parameters, and the fit has 5.5 degrees of freedom. The Event 3 glass data has approximately 14.4 independent parameters, and the fit has 7.4 degrees of freedom.

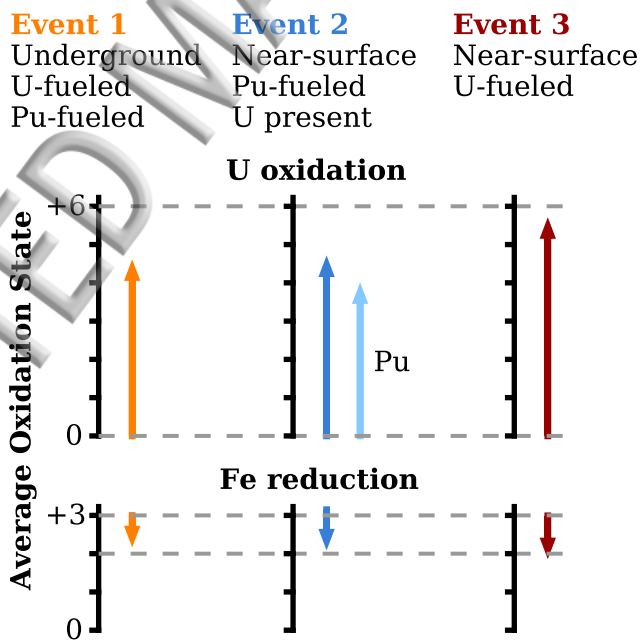

FIG. 10: Summary of changes in oxidation state resulting from each event. Final oxidation states are taken from Tables II and IV. For Event 1 we assume that the predominant initial oxidation state of Fe is Fe(III), on the basis of the oxidation states measured for the Event 2 and Event 3 soils. In all cases we assume that U and Pu are initially metallic.

[1] A. B. Kersting, Inorganic Chemistry **52**, 3533 (2013).

[2] Q. H. Hu, J. Q. Weng, and J. S. Wang, Journal of Environmental Radioactivity **101**, 426 (2010).

[3] J. G. Catalano, S. M. Heald, J. M. Zachara, and G. E. Brown, Environmental Science and Technology **38**, 2822 (2004).

[4] A. F. B. Tompson, C. J. Bruton, G. A. Pawloski, D. K. Smith, W. L. Bourcier, D. E. Shumaker, A. B. Kersting, S. F. Carle, and R. M. Maxwell, Environmental Geology **42**, 235 (2002).

[5] A. Kersting, D. Efurd, D. Finnegan, D. Rokop, D. Smith, and J. Thompson, Nature **397**, 56 (1999).

[6] P. G. Allen, D. K. Shuh, J. J. Bucher, N. M. Edelstein, C. E. A. Palmer, R. J. Silva, S. N. Nguyen, L. N. Marquez, and E. A. Hudson, Radiochimica Acta **75**, 47 (1996).

[7] R. W. Buddemeier and J. R. Hunt, Applied Geochemistry **3**, 535 (1988).

[8] C. Xu, P. H. Santschi, J. Y. Zhong, P. G. Hatcher, A. J. Francis, C. J. Dodge, K. A. Roberts, C. C. Hung, and B. D. Honeyman, Environmental Science and Technology **42**, 8211 (2008).

[9] A. P. Novikov, S. N. Kalmykov, S. Utsunomiya, R. C. Ewing, F. Horreard, A. Merkulov, S. B. Clark, V. V. Tkachev, and B. F. Myasoedov, Science **314**, 638 (2006).

[10] P. H. Santschi, K. A. Roberts, and L. Guo, Environmental Science and Technology **36**, 3711 (2002).

[11] M. J. Apted, G. L. Mcvay, and J. W. Wald, Nuclear Technology **73**, 165 (1985).

[12] Q. H. Hu, T. P. Rose, M. Zavarin, D. K. Smith, J. E. Moran, and P. H. Zhao, Journal of Environmental Radioactivity **99**, 1617 (2008).

[13] A. F. B. Tompson, G. B. Hudson, D. K. Smith, and J. R. Hunt, Advances in Water Resources **29**, 281 (2006).

[14] G. A. Pawloski, A. F. B. Tompson, C. A. Bruton, M. Zavarin, W. L. Bourcier, S. F. Carle, B. K. Esser, A. B. Kersting, R. M. Maxwell, J. A. Rard, et al., Tech. Rep. UCRL-ID-138007-DR (2002).

[15] G. Pohll, A. E. Hassan, J. B. Chapman, C. Papelis, and R. Andricevic, Ground Water **37**, 770 (1999).

[16] I. Y. Borg, Nuclear Technology **26**, 88 (1975).

[17] D. K. Smith, Radiochimica Acta **69**, 157 (1995).

[18] W. S. Cassata, S. G. Prussin, K. B. Knight, I. D. Hutcheon, B. H. Isselhardt, and P. R. Renne, Journal of Environmental Radioactivity **137C**, 88 (2014).

[19] A. J. Fahey, C. J. Zeissler, D. E. Newbury, J. Davis, and R. M. Lindstrom, Proceedings of the National Academy of Sciences **107**, 20207 (2010).

[20] G. R. Eppich, K. B. Knight, T. W. Jacomb-Hood, G. D. Spriggs, and I. D. Hutcheon, Journal of Radioanalytical and Nuclear Chemistry **302**, 593 (2014).

[21] J. J. Bellucci, A. Simonetti, C. Wallace, E. C. Koeman, and P. C. Burns, Analytical Chemistry **85**,

7588 (2013).

[22] E. C. Freiling, Science **133**, 1991 (1961).

[23] S. Glasstone and P. Dolan, *The Effects of Nuclear Weapons* (United States Department of Defense and the Energy Research and Development Administration, Washington, DC, 1977).

[24] G. R. Crocker, J. D. O'Connor, and E. C. Freiling, Health physics **12**, 1099 (1966), ISSN 0017-9078.

[25] K. Maher, J. R. Bargar, and G. E. Brown, Inorganic Chemistry **52**, 3510 (2013), ISSN 00201669.

[26] N. P. Qafoku, J. M. Zachara, C. Liu, P. L. Gassman, O. S. Qafoku, and S. C. Smith, Environmental Science and Technology **39**, 3157 (2005).

[27] D. I. Kaplan, P. M. Bertsch, D. C. Adriano, and K. A. Orlandini, Radiochimica Acta **66-67**, 181 (1994), ISSN 2193-3405.

[28] B. A. Powell, Z. Dai, M. Zavarin, P. Zhao, and A. B. Kersting, Environmental Science & Technology **45**, 2698 (2011), ISSN 0013-936X.

[29] D. E. Crean, F. R. Livens, M. C. Stennett, D. Grolimund, C. N. Borca, and N. C. Hyatt, Environmental Science & Technology **48**, 1467 (2014), ISSN 0013-936X.

[30] T. P. Rose, A. B. Kersting, L. J. Harris, G. B. Hudson, D. K. Smith, R. W. Williams, D. R. Loewen, E. J. Nelson, and J. E. Moran, Tech. Rep. UCRL-ID-154357 (2003).

[31] T. P. Rose, D. K. Smith, and D. L. Phinney, Radiochimica Acta **88**, 465 (2000).

[32] W. E. Jackson, F. Farges, M. Yeager, P. A. Mabrouk, S. Rossano, G. A. Waychunas, E. I. Solomon, and G. E. Brown, Geochimica et Cosmochimica Acta **69**, 4315 (2005).

[33] N. Hess, W. Weber, and S. Conradson, Journal of Nuclear Materials **254**, 175 (1998).

[34] F. Farges, C. W. Ponader, G. Calas, and G. E. Brown, Geochimica et Cosmochimica Acta **56**, 4205 (1992).

[35] D. G. Karraker, Journal of the American Ceramic Society **65**, 53 (1982).

[36] H. D. Schreiber, G. B. Balazs, B. E. Carpenter, J. E. Kirkley, L. M. Minnix, P. L. Jamison, and T. Mason, Journal of the American Ceramic Society **67**, C (1984).

[37] H. D. Schreiber and M. Todd Coolbaugh, Journal of Non-Crystalline Solids **181**, 225 (1995).

[38] H. D. Schreiber, Journal of Non-Crystalline Solids **84**, 129 (1986).

[39] M. W. Medlin, K. D. Sienerth, and H. D. Schreiber, Journal of Non-Crystalline Solids **240**, 193 (1998).

[40] H. D. Schreiber, Journal of the Less Common Metals **91**, 129 (1983).

[41] H. D. Schreiber, B. K. Kochanowski, C. W. Schreiber, A. B. Morgan, M. Coolbaugh, and T. G. Dunlap, Journal of Non-Crystalline Solids **177**, 340 (1994).

[42] H. D. Schreiber, B. E. Carpenter, J. P. Eckenrode, and G. B. Balazs, Physics and Chemistry of Glasses **26**, 24 (1985).

[43] G. Giuli, G. Pratesi, S. G. Eeckhout, and E. Paris, in *Large Meteorite Impacts and Planetary Evolution IV* (Geological Society of America, 2010), vol. 465 of *Geological Society of America Special Papers*, ISBN 978-0-8137-2465-2.

[44] A. A. Sheffer, Ph.D. thesis, The University of Arizona (2007).

[45] http://lise.lbl.gov/RSXAP/, accessed: 2015-08-13.

[46] G. G. Li, F. Bridges, and C. H. Booth, Physical Review B **52**, 6332 (1995).

[47] T. Hayes and J. Boyce, *Solid State Physics*, vol. 37 (Academic, New York, 1982).

[48] A. L. Ankudinov, B. Ravel, J. J. Rehr, and S. D. Conradson, Physical Review B **58**, 7565 (1998).

[49] C. H. Booth and Y.-J. Hu, Journal of Physics: Conference Series **190**, 012028 (2009).

[50] G. Giuli, M. R. Cicconi, S. G. Eeckhout, G. Pratesi, E. Paris, and L. Folco, Meteoritics and Planetary Science **49**, 696 (2014).

[51] A. J. Berry, H. S. C. O'Neill, K. D. Jayasuriya, S. J. Campbell, and G. J. Foran, American Mineralogist **88**, 967 (2003).

[52] G. Giuli, G. Pratesi, C. Cipriani, and E. Paris, Geochimica et Cosmochimica Acta **66**, 4347 (2002).

[53] E. Cottrell, K. A. Kelley, A. Lanzirotti, and R. A. Fischer, Chemical Geology **268**, 167 (2009).

[54] M. Wilke, G. M. Partzsch, R. Bernhardt, and D. Lattard, Chemical Geology **220**, 143 (2005).

[55] M. Wilke, F. Farges, and P. Petit, American Mineralogist 86, 714 (2001).

[56] M. Bonnin-Mosbah, A. S. Simionovici, N. Métrich, J. P. Duraud, D. Massare, and P. Dillmann, Journal of Non-Crystalline Solids **288**, 103 (2001).

[57] S. Bajt, S. Sutton, and J. Delaney, Geochimica et Cosmochimica Acta **58**, 5209 (1994).

[58] F. de Groot, Coordination Chemistry Reviews **249**, 31 (2005), ISSN 00108545.

[59] T. E. Westre, P. Kennepohl, J. G. DeWitt, B. Hedman, K. O. Hodgson, and E. I. Solomon, Journal of the American Chemical Society **119**, 6297 (1997), ISSN 0002-7863.

[60] F. Farges, Physics and Chemistry of Minerals **28**, 619 (2001).

[61] D. R. Chapman and L. C. Scheiber, Journal of Geophysical Research **74**, 6737 (1969).

[62] G. Giuli, S. G. Eeckhout, M. R. Cicconi, and E. Paris, in *Large Meteorite Impacts and Planetary Evolution IV* (Geological Society of America, 2010), vol. 465 of *Geological Society of America Special Papers*, ISBN 978-0-8137-2465-2.

[63] L. Wang, A. Yoshiasa, M. Okube, T. Hiratoko, Y. Hu, H. Arima, and K. Sugiyama, Journal of Mineralogical and Petrological Sciences **108**, 288 (2013).

[64] C. M. B. Henderson, J. M. Charnock, J. V. Smith, and G. N. Greaves, American Mineralogist **78**, 477 (1993).

[65] P. G. Allen, J. J. Bucher, D. K. Shuh, N. M. Edelstein, and T. Reich, Inorganic Chemistry **36**, 4676 (1997).

[66] J. Selbin and J. D. Ortego, Chemical Reviews **69**, 657 (1969).

[67] H. D. Schreiber, Journal of Non-Crystalline Solids **42**, 175 (1980).

[68] F. Belloni, J. Himbert, O. Marzocchi, and V. Romanello, Journal of Environmental Radioactivity **102**, 852 (2011).

[69] C. Guéneau, M. Baichi, D. Labroche, C. Chatillon, and B. Sundman, Journal of Nuclear Materials **304**, 161 (2002), ISSN 00223115.

[70] P.-Y. Chevalier, E. Fischer, and B. Cheynet, Journal of Nuclear Materials **303**, 1 (2002), ISSN 00223115.

[71] G. Calas, Geochimica et Cosmochimica Acta **43**, 1521 (1979).

[72] H. D. Schreiber, G. B. Balazs, P. L. Jamison, and A. P. Shaffer, Physics and chemistry of glasses **23**, 147 (1982).

[73] T. Widner, Tech. Rep. LAHRDA (2010).

[74] G. N. Eby, N. Charnley, D. Pirrie, R. Hermes, J. Smoliga, and G. Rollinson, American Mineralogist **100**, 427 (2015).

[75] M. C. Duff, J. U. Coughlin, and D. B. Hunter, Geochimica et Cosmochimica Acta **66**, 3533 (2002).

[76] D. E. Giammar and J. G. Hering, Environmental Science and Technology **35**, 3332 (2001).

[77] E. Sylwester, E. Hudson, and P. Allen, Geochimica et Cosmochimica Acta **64**, 2431 (2000).

[78] L. Morss, M. Lewis, M. Richmann, and D. Lexa, Journal of Alloys and Compounds **303-304**, 42 (2000).

[79] J. D. Begg, M. Zavarin, P. Zhao, S. J. Tumey, B. Powell, and A. B. Kersting, Environmental Science and Technology **47**, 5146 (2013).

[80] M. C. Duff, D. B. Hunter, I. R. Triay, P. M. Bertsch, D. T. Reed, S. R. Sutton, G. Shea-Mccarthy, J. Kitten, P. Eng, S. J. Chipera, et al., Environmental Science and Technology **33**, 2163 (1999).

[81] S. Utsunomiya, A. B. Kersting, and R. C. Ewing, Environmental Science and Technology **43**, 1293 (2009).

[82] C. H. Booth, P. G. Allen, J. J. Bucher, N. M. Edelstein, D. K. Shuh, G. K. Marasinghe, M. Karabulut, C. S. Ray, and D. E. Day, Journal of Materials Research **14**, 2628 (1999).

[83] E. A. Stern, Physical Review B **48**, 9825 (1993).

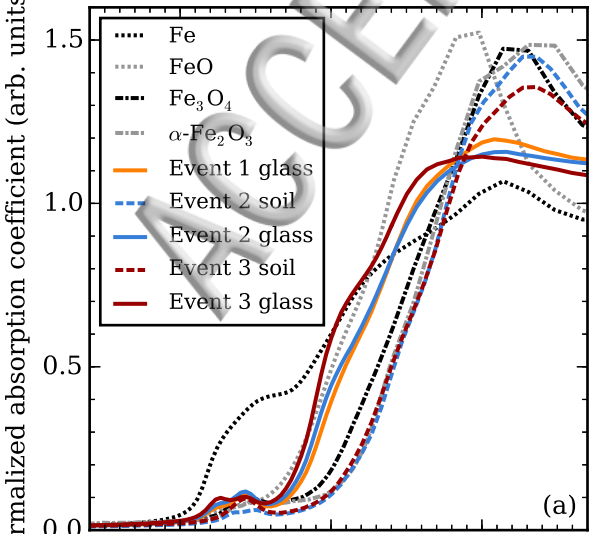
Fe
FeO
Fe_3O_4
α-Fe_2O_3
Event 1 glass
Event 2 soil
Event 2 glass
Event 3 soil
Event 3 glass
Normalized absorption coefficient (arb. units)
Energy (eV)
(a)
0.0
0.5
1.0
1.5
7110
7120
7130

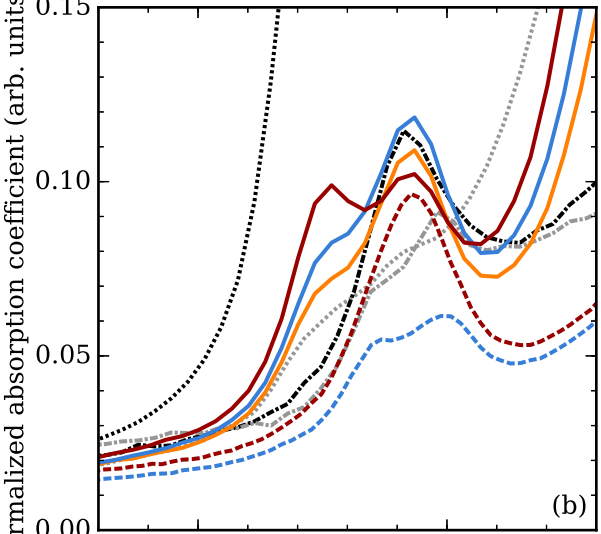
Normalized absorption coefficient (arb. units)
Energy (eV)
(b)
0.00
0.05
0.10
0.15
7110
7115

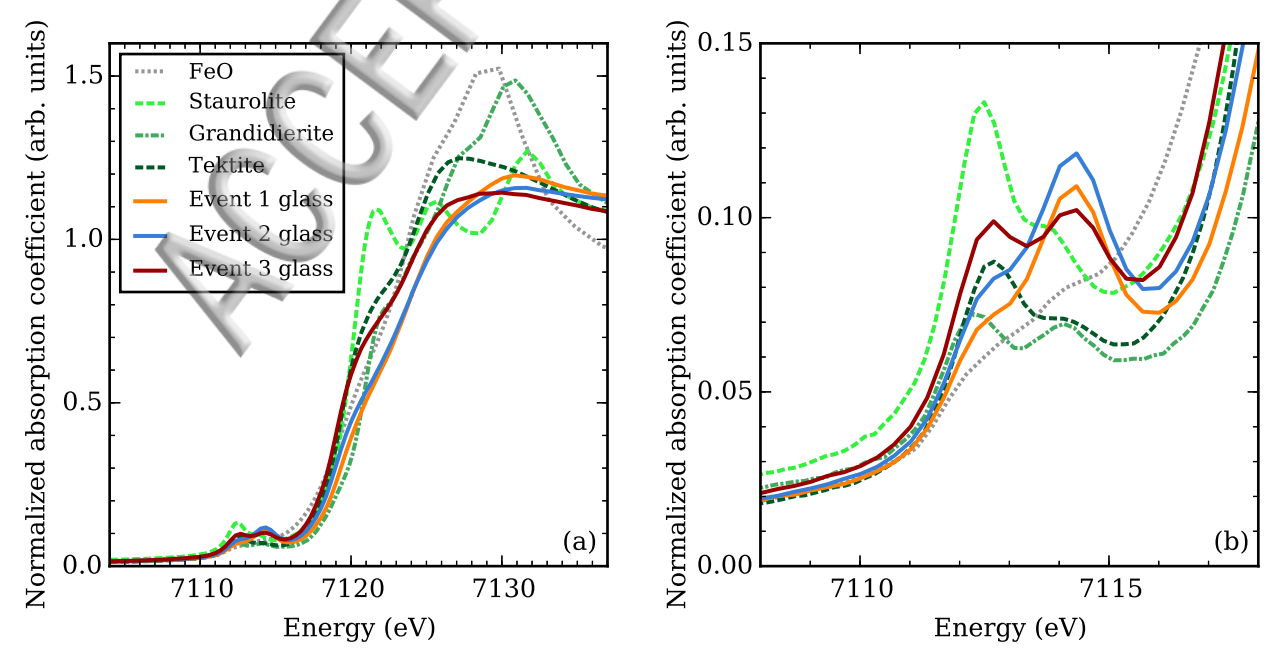
FeO
Staurolite
Grandidierite
Tektite
Event 1 glass
Event 2 glass
Event 3 glass
Normalized absorption coefficient (arb. units)
Energy (eV)
(a)
(b)
0.0
0.5
1.0
1.5
0.00
0.05
0.10
0.15
7110
7120
7130
7115

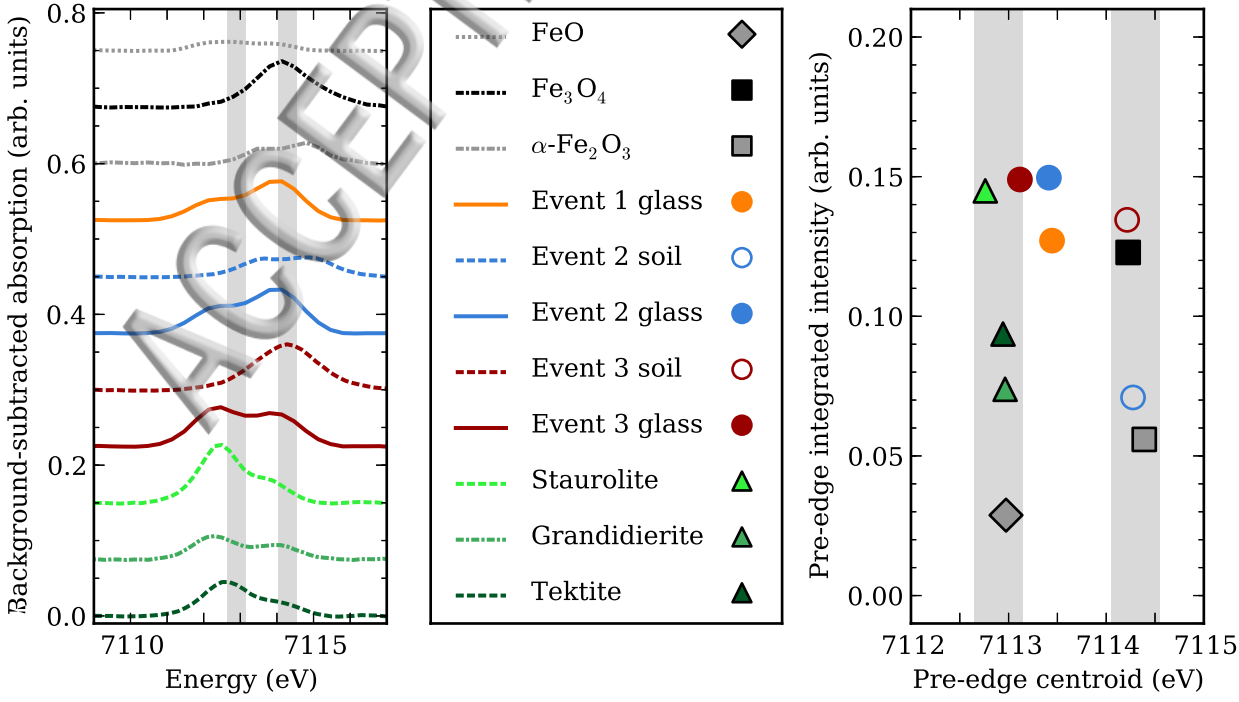
Background-subtracted absorption (arb. units)
0.0
0.2
0.4
0.6
0.8
7110
7115
Energy (eV)
FeO
Fe_3O_4
α-Fe_2O_3
Event 1 glass
Event 2 soil
Event 2 glass
Event 3 soil
Event 3 glass
Staurolite
Grandidierite
Tektite
Pre-edge integrated intensity (arb. units)
0.00
0.05
0.10
0.15
0.20
7112
7113
7114
7115
Pre-edge centroid (eV)

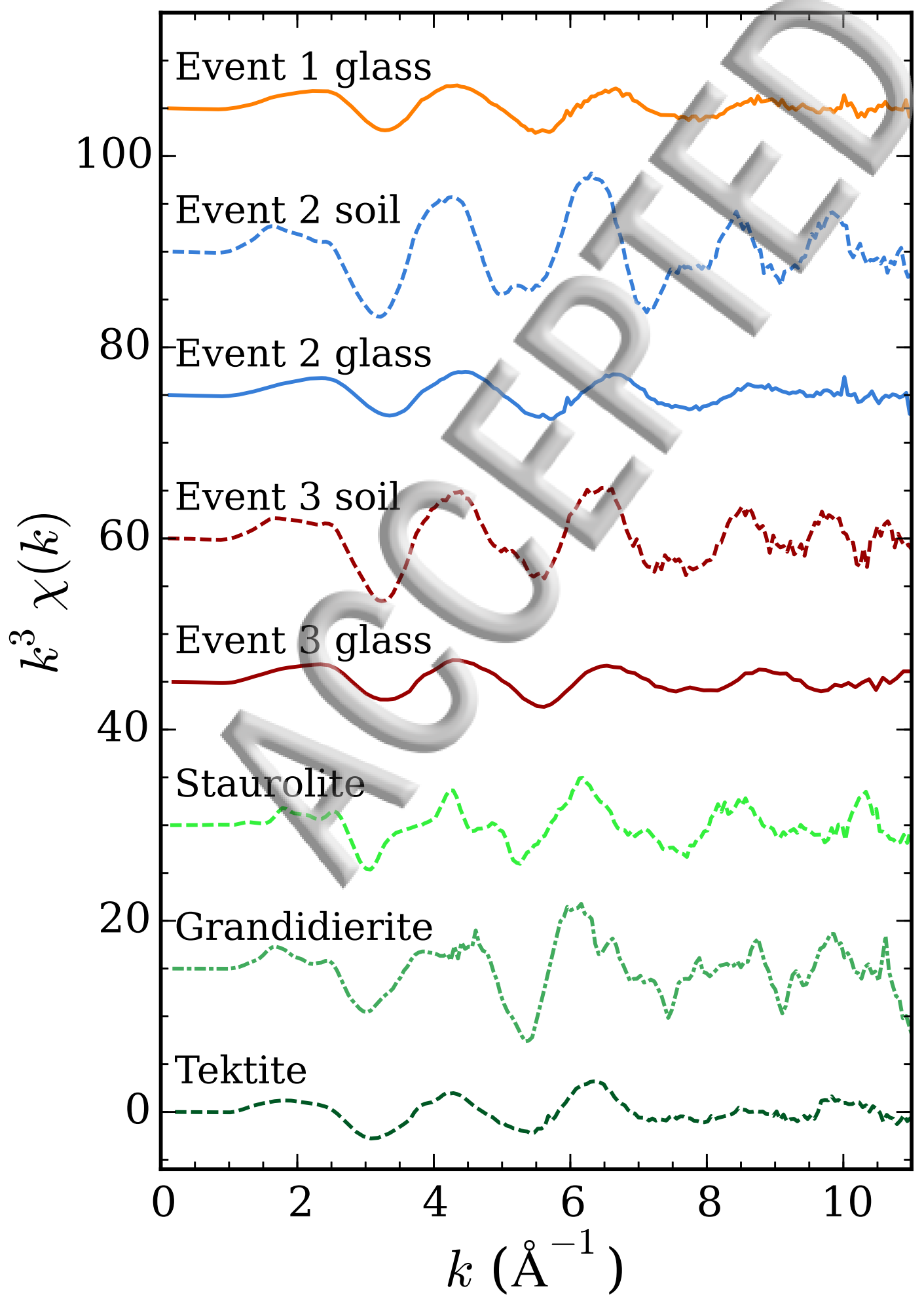
Event 1 glass
Event 2 soil
Event 2 glass
Event 3 soil
Event 3 glass
Staurolite
Grandidierite
Tektite
100
80
60
40
20
0
0
2
4
6
8
10
$k^3\ \chi(k)$
k (Å^{-1})
ACCEPTED

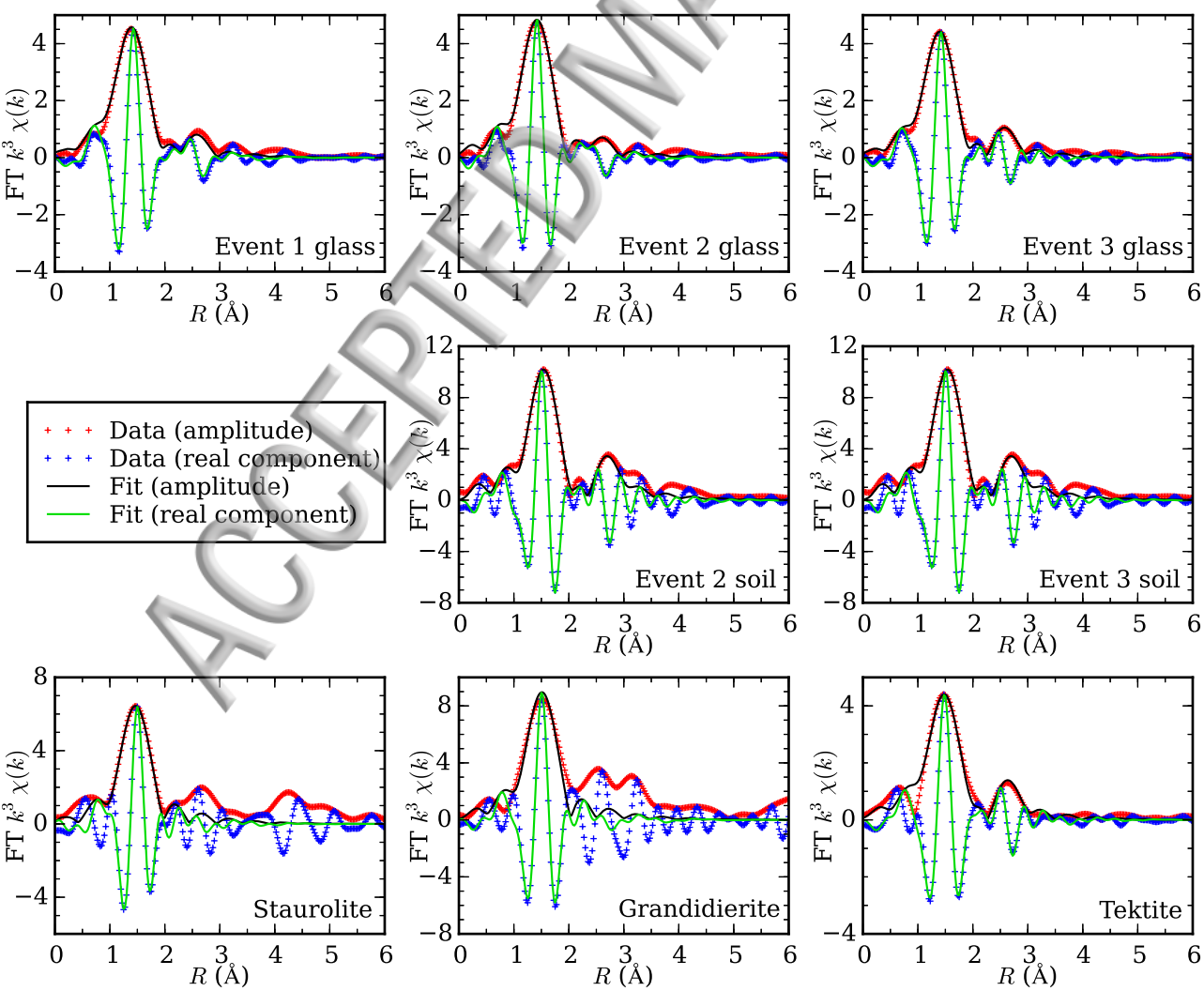
Event 1 glass
Event 2 glass
Event 3 glass
Event 2 soil
Event 3 soil
Staurolite
Grandidierite
Tektite
Data (amplitude)
Data (real component)
Fit (amplitude)
Fit (real component)
FT k^3 $\chi(k)$
R (Å)

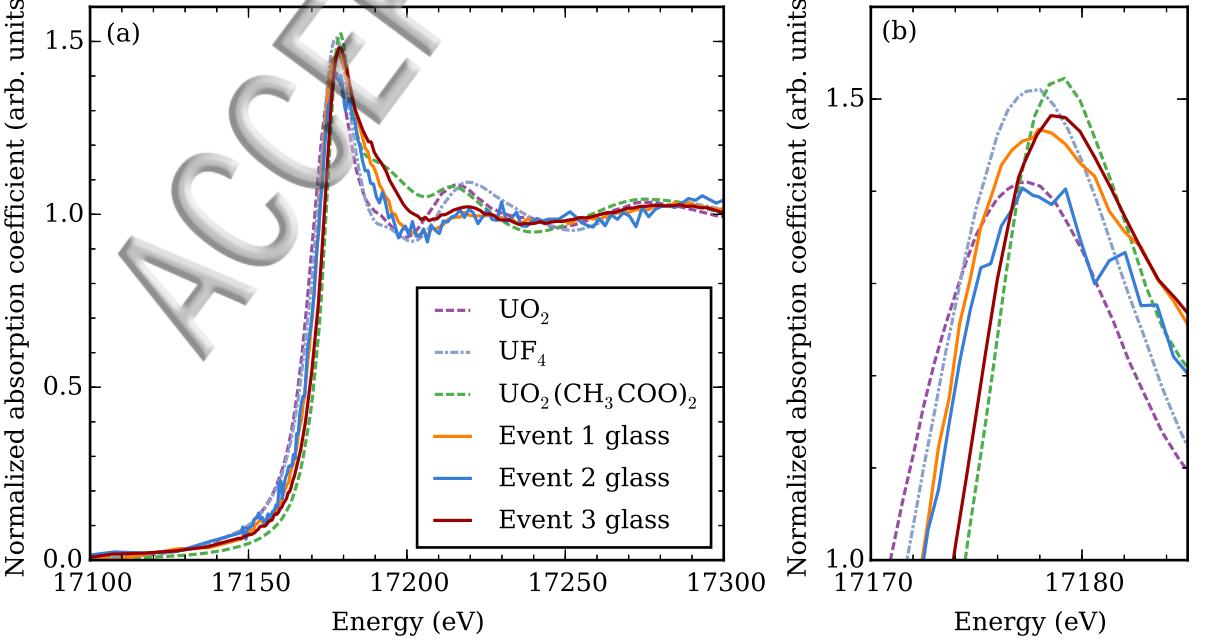
(a)
(b)
Normalized absorption coefficient (arb. units)
Energy (eV)
0.0
0.5
1.0
1.5
17100
17150
17200
17250
17300
17170
17180
UO_2
UF_4
$UO_2(CH_3COO)_2$
Event 1 glass
Event 2 glass
Event 3 glass

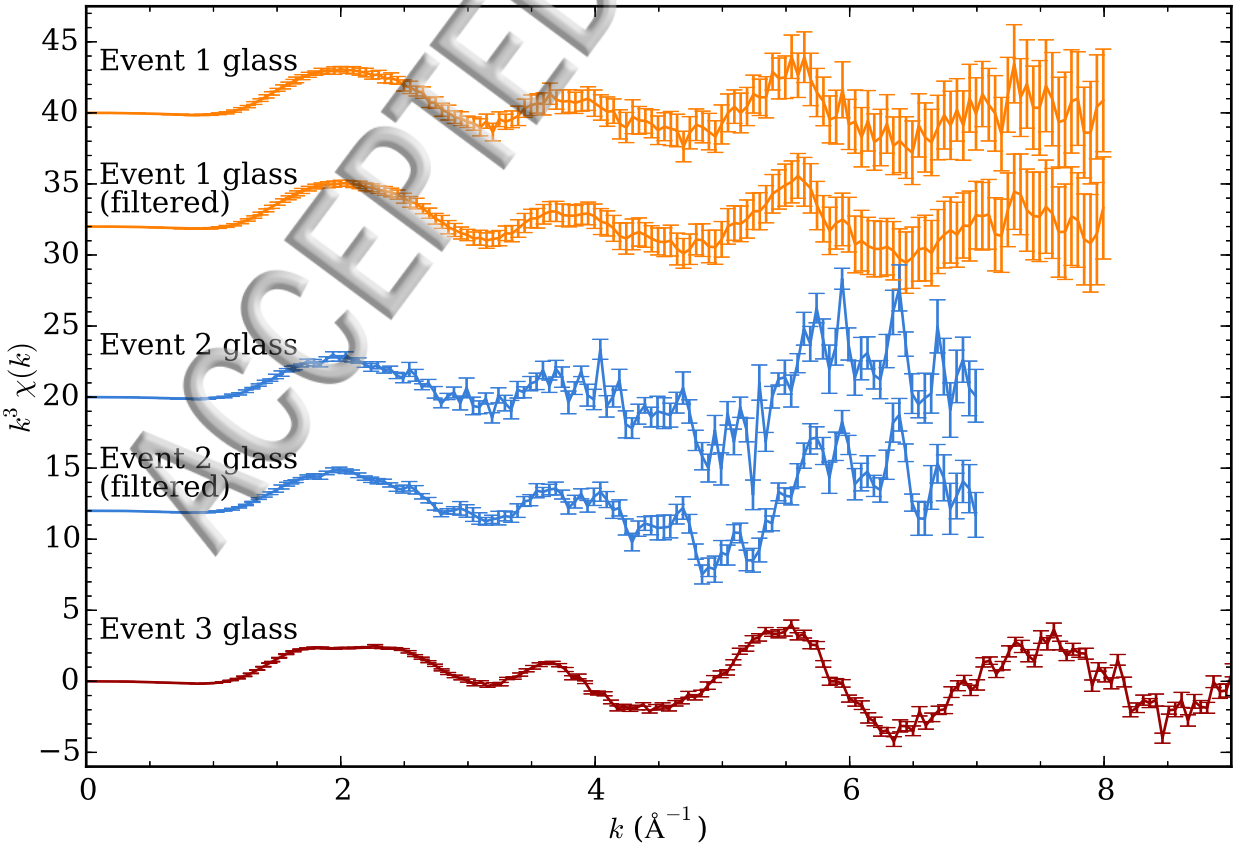
Event 1 glass
Event 1 glass (filtered)
Event 2 glass
Event 2 glass (filtered)
Event 3 glass
$k^3\,\chi(k)$
k (Å^{-1})
45
40
35
30
25
20
15
10
5
0
−5
0
2
4
6
8

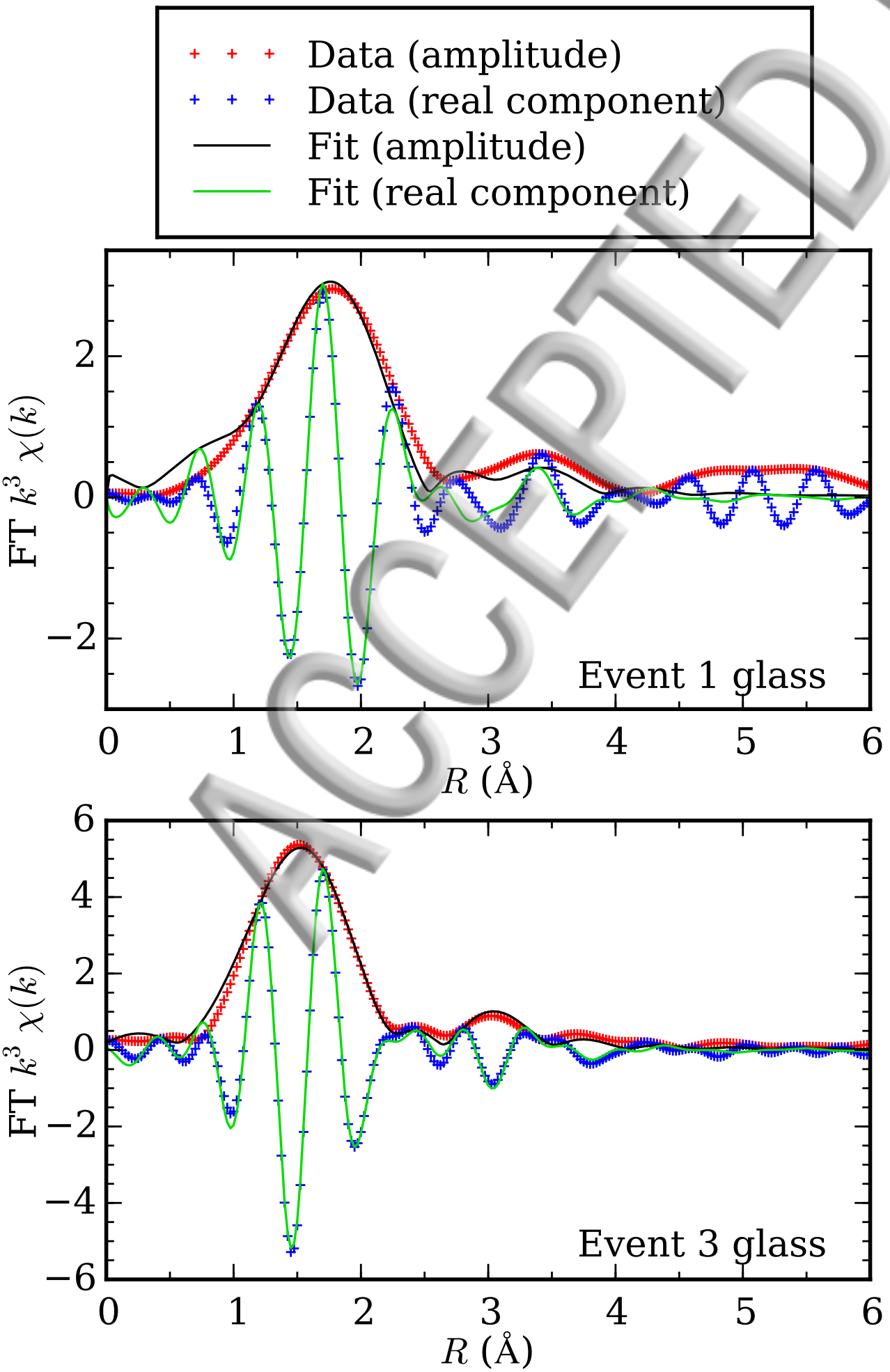
Data (amplitude)
Data (real component)
Fit (amplitude)
Fit (real component)
FT k^3 $\chi(k)$
Event 1 glass
R (Å)
FT k^3 $\chi(k)$
Event 3 glass
R (Å)

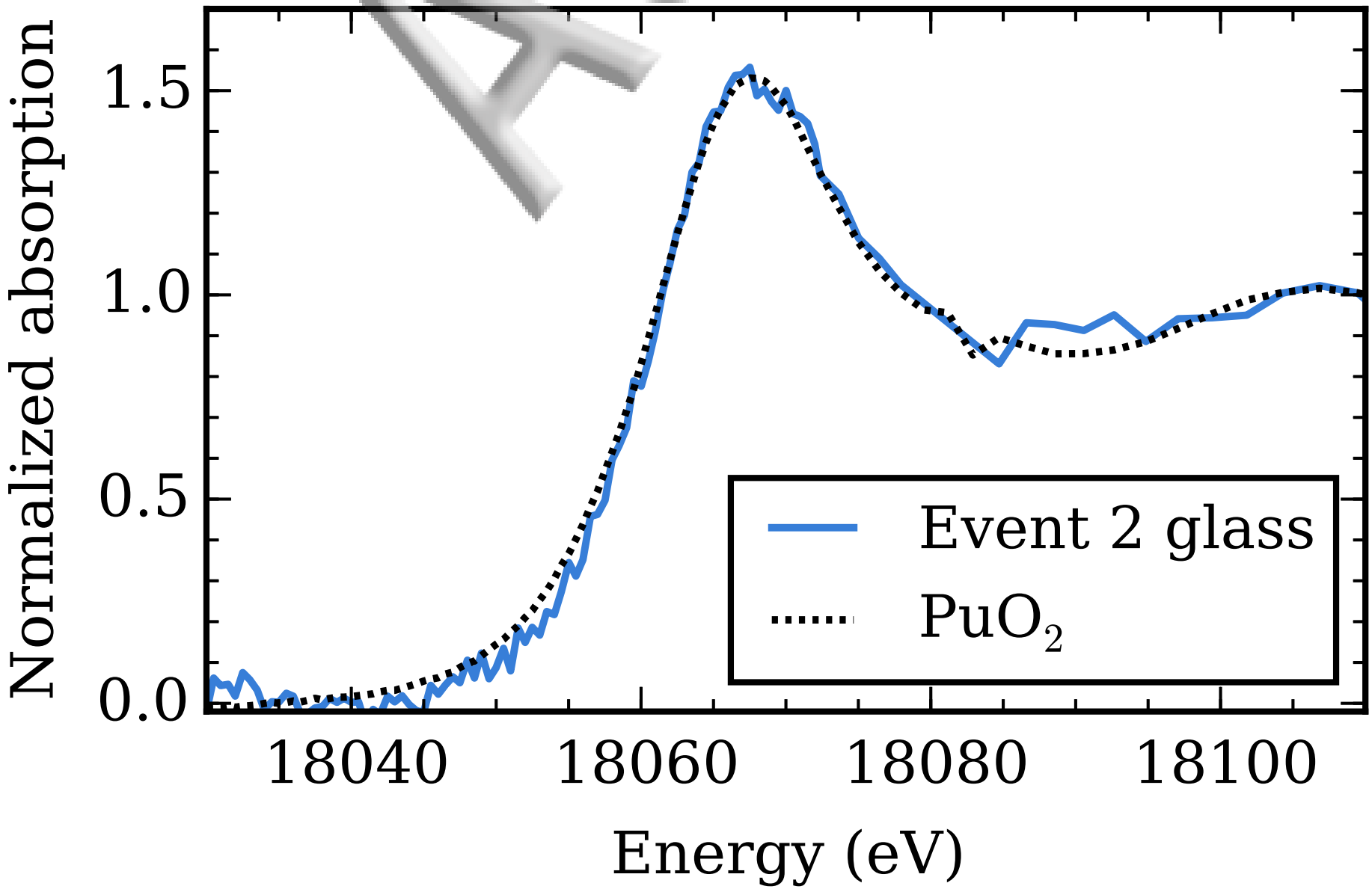
Normalized absorption
1.5
1.0
0.5
0.0
18040
18060
18080
18100
Energy (eV)
Event 2 glass
PuO2

Event 1
Underground
U-fueled
Pu-fueled

Event 2
Near-surface
Pu-fueled
U present

Event 3
Near-surface
U-fueled